FRONTIERS OF PHYSICS

RESEARCH ARTICLE
Volume 21 / Issue 12 / 125203 / 2026

Prediction of a multifunctional hexagonal Fe_2O_3 monolayer with chiral antiferromagnetism and piezoelectricity

Qi Wang[1], Junyuan Wang[1], Xu Yan[1,2,†], Guochun Yang[1,‡]

1 State Key Laboratory of Metastable Materials Science & Technology and Hebei Key Laboratory of Microstructural Material Physics, School of Science, Yanshan University, Qinhuangdao 066004, China
2 College of Physics and Hebei Advanced Thin Films Laboratory, Hebei Normal University, Shijiazhuang 050024, China
Corresponding authors. E-mail: †xuyan980504@163.com, ‡yanggc468@nenu.edu.cn
Received December 17, 2025; accepted March 27, 2026

ABSTRACT

Two-dimensional (2D) materials that exhibit magnetism and piezoelectricity offer exciting opportunities for next-generation spintronic and multifunctional devices. The recently synthesized 2D hexagonal Fe_2O_3 provides a promising platform [*Nat. Mater.* 20, 1073 (2021)], yet its atomic structure remains unidentified. Herein, we report that high-throughput first-principles screening reveals a viable monolayer structure that can serve as a candidate for experimental realization. The proposed hexagonal Fe_2O_3 monolayer features a large direct band gap of 3.1 eV and hosts a robust chiral antiferromagnetic order stabilized by the interplay between triangular-lattice-induced geometric frustration and strong magnetic anisotropy. The absence of inversion symmetries gives rise to a pronounced in-plane piezoelectric response, with a d_{11} coefficient of –29.51 pm/V. Remarkably, these key electronic, magnetic, and piezoelectric properties remain robust under biaxial strain, highlighting the hexagonal Fe_2O_3 monolayer as a multifunctional candidate for piezoelectrically engineered spintronic applications.

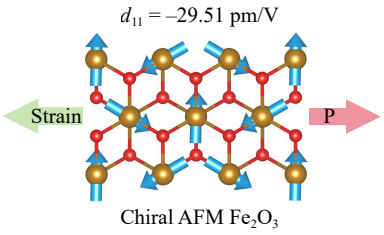

Keywords chiral AFM Fe_2O_3 monolayer, magnetic anisotropy energy, biaxial strain, piezoelectric effect, first-principles calculations

1 Introduction

Two-dimensional (2D) magnetic materials have rapidly emerged as a vibrant research frontier owing to their fundamental scientific significance and potential device applications [1–4]. Unlike their bulk counterparts, magnetic order in 2D systems arises from the interplay between reduced dimensionality, exchange interactions, and magnetic anisotropy, which stabilizes long-range spin alignment against thermal fluctuations even in monolayers [5]. A broad spectrum of 2D magnets, including ferromagnets [6–9], ferrimagnets [10, 11], and antiferromagnets [12–14], has been discovered, each exhibiting distinct spin configurations and tunable magnetic properties. Recent advances have revealed rich physical phenomena in two-dimensional magnetic materials, including multiferroicity, valley polarization, and altermagnetic behavior [15–18]. Among these, antiferromagnetic (AFM) materials, characterized by antiparallel spin alignment and vanishing net magnetization, offer unique advantages such as negligible stray fields and ultrafast spin dynamics, rendering them ideal platforms for next-generation high-speed and high-density spintronic devices [19–21]. Moreover, the pronounced sensitivity of

https://doi.org/10.15302/frontphys.2026.125203

2D magnets to external stimuli such as electric fields or strain enables strong magnetoelectric coupling, opening promising avenues for investigating microscopic mechanisms and designing multifunctional spintronic architectures.

In triangular lattices, intrinsic magnetic exchange frustration often gives rise to noncollinear spin configurations. In particular, the 120° coplanar chiral AFM order has drawn particular attention because it simultaneously breaks time-reversal symmetry [22, 23]. Such chiral spin textures underpin a broad spectrum of emergent quantum phenomena including spin-liquid behavior, improper ferroelectric polarization, magnetoelectric coupling, anomalous Hall effects, and topological spin structures [24–26], many of which have been experimentally observed in materials such as Mn_3Pt [27] and $NiGa_2S_4$ [28]. With the rapid advancement of 2D magnetism, room-temperature-stable chiral AFM order has recently been realized in layered systems such as $Hf_2VC_2F_2$ [29], marking an important step toward integrating frustrated magnetism into low-dimensional materials. Notwithstanding significant progress, genuinely robust chiral AFM in the atomically thin limit remains scarce. Achieving this goal hinges on a fundamental understanding of the synergy between magnetic frustration and anisotropy in reduced dimensions, underscoring the imperative to explore intrinsically frustrated 2D magnets with strong anisotropy and tunable coupling.

On the other hand, achieving efficient and low-power electric-field switching remains a major challenge for practical applications. Conventional ferroelectric strategies suffer from hysteresis, fatigue, and limited switching speeds, which restrict their reliability and scalability [30]. Piezoelectric strain engineering offers an alternative route by exploiting noncentrosymmetric materials to convert external voltages into linear, hysteresis-free, and ultrafast in-plane strains. These strains can directly and efficiently tune magnetic order through magnetoelastic coupling, providing a robust and energy-efficient means of electric-field-driven magnetic control. 2D piezoelectrics further enhance this capability owing to their flexibility, large surface-to-volume ratio, and strong surface charge response, leading to remarkable piezoelectric efficiencies [31–34]. For example, monolayer MoS_2 exhibits a piezoelectric coefficient of about 3.71 pm/V [35, 36], comparable to bulk α-quartz [37], while the predicted d_{22} of monolayer SnSe can reach approximately 250 pm/V [38]. These exceptional properties position 2D piezoelectrics as key enablers for the next generation of energy-efficient and tunable electronic devices.

Fe-based 2D magnets have attracted significant attention due to their abundance, environmental benignity, and technological compatibility. Typical examples such as $FePS_3$ [12], FeSe [39], Fe_3GeTe_2 [7], Fe_3GaTe_2 [40], Fe_2O_3 [41], Fe_3O_4 [42], and FeO_2 [43] exhibit rich crystal configurations alongside diverse magnetic and electronic properties, making them model systems for investigating spin, charge, and orbital coupling phenomena. Recently, 2D hexagonal Fe_2O_3 was experimentally synthesized, though its precise crystal structure remains unresolved. Here, high-throughput structural screening identifies an possible experimental hexagonal Fe_2O_3 monolayer with Fe ions forming a triangular lattice. This phase exhibits a large magnetic anisotropy energy of 3.88 meV/Fe, stabilizing a chiral AFM order robust under –6% to 2% biaxial strain, and an exceptionally high, strain-tunable piezoelectric coefficient d_{11}, modifiable by more than a factor of two. These results provide a concrete material target and a theoretical foundation for piezoelectrical AFM spintronic devices.

2 Results and discussion

Experimentally, Fe_2O_3 has been confirmed to adopt a hexagonal symmetry, although the precise atomic positions remain unresolved [44]. Based on the 2:3 stoichiometry, we performed a high-throughput screening of binary compounds with hexagonal structures from the C2DB [45] materials database, considering both interatomic interactions and chemical bonding rationality. Twelve candidate parent structures with potential stability were thus identified. The dynamical stability of the structure was assessed by phonon spectrum calculations (see Supplementary Materials Fig. S1). Among these, one structure [Fig. 1(a)] emerged as the energetically most favorable and exhibited no imaginary frequencies in its phonon spectrum [Fig. 1(b)]. The simulated high-resolution transmission electron microscopy (HRTEM) image of this configuration shows a distinct hexagonal pattern, consistent with observations (see Supplementary Materials Fig. S2) [46], offering strong evidence for its validity as the experimental 2D Fe_2O_3. Structurally, the monolayer consists of an O–Fe–O–Fe–O stacking sequence, where Fe atoms form a triangular lattice within sublayers. Each Fe atom is bonded to six surrounding O atoms, resulting in distorted FeO_6 octahedral characteristic of the hexagonal lattice framework. Slight structural deformation after 5 ps AIMD simulations at 300 K demonstrates thermal stability [Fig. 1(c)]. Mechanical stability is evidenced by the elastic constants, which satisfy C_{11}, $C_{12} > 0$ and $C_{11} > |C_{12}|$. The monolayer exhibits isotropic mechanical behaviors, as shown in Figs. 1(e) and (f), with a Young's modulus of 100 N/m, a value that lies between those of MoS_2 monolayer (120.10 N/m) [47] and black phosphorus (92.13 N/m) [48], and a Poisson's ratio of approximately 0.6, indicating a large capacity for lateral deformation.

To determine the magnetic ground state of the Fe_2O_3 monolayer, we systematically considered six representative magnetic configurations [Fig. 2]. The collinear configurations are selected to include both FM and AFM coupling

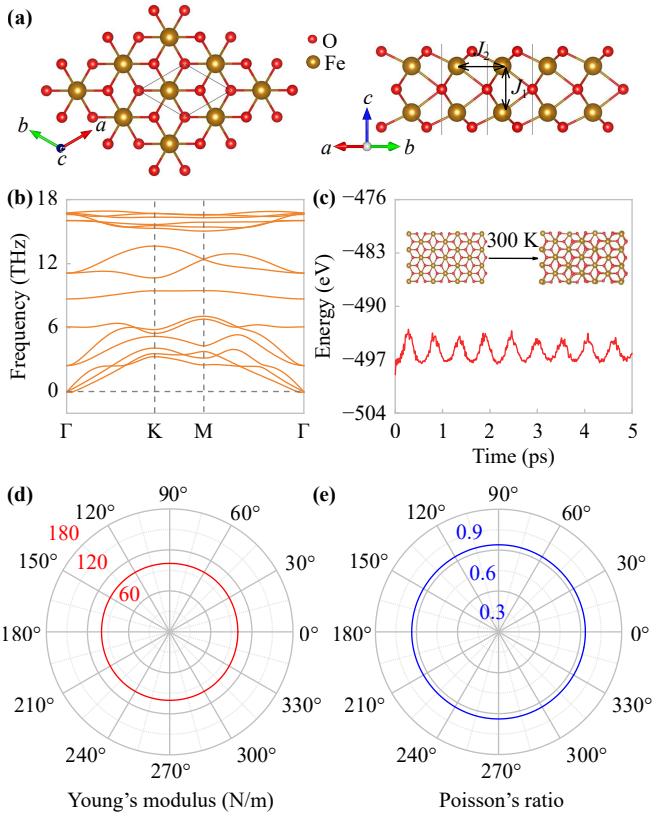

Fig. 1 **(a)** Top and side views, **(b)** phonon dispersion curves, **(c)** snapshot and energy from molecular dynamics simulation at 300 K, **(d)** orientation-dependent Young's modulus, and **(e)** orientation-dependent Poisson's ratio of the Fe_2O_3 monolayer.

states between in-plane and out-of-plane nearest-neighbor Fe ions. In addition, the 120° chiral AFM state is included to capture the key noncollinear order arising from geometric frustration in this system. Energy comparisons of these magnetic configurations indicate that the Fe_2O_3 monolayer adopts a chiral AFM ground state, characterized by interlayer FM coupling and intralayer 120° coplanar AFM spin arrangements. In octahedral ligand field [Fig. 3(a)], the Fe $3d$ orbitals split into triply degenerate t_{2g} states (d_{xy}, d_{xz}, and d_{yz}) and doubly degenerate e_g states ($d_{x^2-y^2}$ and d_{z^2}). The half-filled Fe $3d$ orbitals contribute a large magnetic moment of 5 μ_B/Fe.

Moreover, the chiral AFM Fe_2O_3 monolayer possesses easy-plane magnetization with a sizeable magnetic anisotropy energy (MAE) of 3.88 meV/Fe [Fig. 3(b)], which is significantly larger than that of the CrI_3 monolayer (~0.84 meV/Cr) [49] and ensures robust in-plane magnetization. The large MAE, zero net magnetization, and frustration-stabilized spin chirality ensure robustness of spin arrangement against small perturbations, although minor spin canting cannot be entirely excluded. The orbital-resolved analysis of the magnetic anisotropy energy (MAE) within the framework of second-order perturbation theory is shown in Fig. S3. The calculated magnetic shape anisotropy of 0.394 meV/Fe also favors in-plane magnetization. The preference for in-plane magnetization is maintained across U values ranging from 4.00 to 7.89 eV (Table S2).

To reveal the temperature-dependent magnetism, the coupling strength between Fe atoms was analyzed using the Heisenberg spin Hamiltonian:

$$\mathrm{H} = -\sum_{\langle ij \rangle} J_1 \boldsymbol{S}_i \boldsymbol{S}_j - \sum_{\langle mn \rangle} J_2 \boldsymbol{S}_m \boldsymbol{S}_n - A \sum_i \left(S_i^{ab}\right)^2. \quad (1)$$

Here, J_1 and J_2 represent the interlayer nearest-neighbor (NN) and intralayer next-nearest-neighbor (NNN) exchange interaction, respectively [Figs. 1(a) and S4], $\langle ij \rangle$ and $\langle mn \rangle$ correspond to the site of NN and NNN Fe ions, respectively, S is the normalized spin operator, taken as 5/2 here, S_i^{ab} represents the in-plane spin component magnitude of Fe ion at i site, defined as

$$S_i^{ab} = \sqrt{\left(S_i^x\right)^2 + \left(S_i^y\right)^2}, \quad (2)$$

where S_i^x and S_i^y are the components of the spin operator along the in-plane x- and y-directions, respectively. A is the magnetocrystalline anisotropy coefficient. The J_1 and J_2 are calculated to be 0.84 and –2.80 meV. The positive J_1 indicates interlayer FM coupling, whereas the negative J_2, which dominates the in-plane interactions, originates from the geometric frustration inherent in the triangular lattice. In this lattice, the geometry leads to magnetic frustration, preventing the simultaneous satisfaction of antiparallel alignment among all three neighboring magnetic atoms in an AFM Néel state [43, 50]. Consequently, the ground state stabilizes into a chiral AFM order characterized by a magnetic propagation vector $\boldsymbol{q} = (\pi/3, \pi/3, 0)$.

Monte Carlo simulations based on the Heisenberg model at different temperatures determined that the chiral AFM order in the Fe_2O_3 monolayer can persist below a Néel temperature (T_N) of 40 K, higher than the previously reported 2D non-collinear materials, such as $MnRe_2O_8$ monolayers (31 K) [51] and MnSi monolayers (27.7 K) [52]. Figures 3(c)–(e) show the real-space distribution of magnetic moments at different temperatures. At 10 K, the spin directions in the triangular lattice mainly remain within the ab-plane, exhibiting a spin-frustrated state with a 120° angle between adjacent Fe atoms. When the temperature rises to 40 K, the spin-frustrated state persists (see Supplementary Materials Fig. S5). As the temperature rises above 40 K, the 120° spin order between in-plane neighbors degrades, and the parallel alignment of spins between adjacent layers is progressively destroyed, showing a clear trend toward interlayer decoupling. At 200 K, disordered regions dominate the entire lattice, and the Fe_2O_3 monolayer transitions to a paramagnetic state. The magnetic

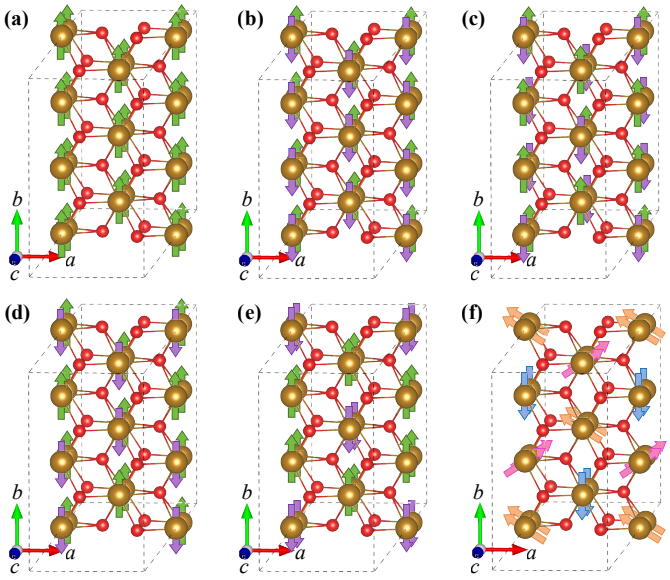

Fig. 2 Magnetic configurations of the Fe_2O_3 monolayer, **(a)** FM, **(b)** AFM1, **(c)** AFM2, **(d)** FIM1, **(e)** FIM2, and **(f)** chiral AFM. Green and purple arrows indicate spin-up and spin-down, respectively, while blue, pink, and orange arrows represent 120° coplanar spin directions.

moment snapshots with the U values ranging from 4 to 7 eV are shown in Fig. S6, and the corresponding J values are provided in Table S3.

To investigate the spin-related physical properties in the chiral AFM Fe_2O_3 monolayer, we calculated the spin-resolved band structure with considering SOC. The Fe_2O_3 monolayer is a semiconductor with a direct band gap of 3.10 eV [Figs. 3(f)–(h)]. Such a wide gap ensures its semiconducting behavior at room temperature. Furthermore, the x, y, and z magnetization components exhibit highly non-trivial distribution patterns in momentum space. Specifically, As the k-point traverses the high-symmetry path M→K→Γ, the intensity of the spin z-component gradually increases, while the spin intensities of other components gradually decrease and even change sign. This characteristic, where the spin direction undergoes continuous, smooth, and large-amplitude rotation with momentum, is direct evidence of "non-trivial spin-momentum locking" and a hallmark electronic structure feature of such coplanar antiferromagnets under strong SOC [53]. This phenomenon indicates an intimate coupling between spin and orbital degrees of freedom, providing the intrinsic structural basis for potential emerging transport properties like the anomalous Hall effect [26].

The non-centrosymmetric Fe_2O_3 structure and intrinsic semiconducting feature allow the piezoelectric effect. Here, a $\sqrt{3} \times 3 \times 1$ supercell was selected for piezoelectricity calculations [Fig. 2(f)]. The polarization induced by strain or stress in non-centrosymmetric crystals can be characterized by third-rank piezoelectric strain (e_{ijk}) and stress (d_{ijk}) tensors. The piezoelectric tensor can be characterized by the first-order derivative, with specific equations:

$$e_{ijk} = \frac{\partial P_i}{\partial \varepsilon_{jk}} = e_{ijk}^{\text{elec}} + e_{ijk}^{\text{ion}}, \tag{3}$$

$$d_{ijk} = \frac{\partial P_i}{\partial \varepsilon_{jk}} = d_{ijk}^{\text{elec}} + d_{ijk}^{\text{ion}}. \tag{4}$$

Here, P_i, ε_{jk}, and σ_{jk} represent the polarization vector, strain, and stress, respectively. i, j, and k correspond to the x, y, and z directions. The sum of the piezoelectric stress and strain tensors reflects the ionic and electronic contributions. The piezoelectric coefficients e_{ijk} and d_{imn} are related to the elastic tensor C_{mnjk}:

$$e_{ijk} = \left(\frac{\partial P_i}{\partial \varepsilon_{jk}}\right)\left(\frac{\partial P_i}{\partial \sigma_{jk}}\right) = d_{imn} C_{mnjk}. \tag{5}$$

For the Fe_2O_3 monolayer, it can be simplified by considering only in-plane strain and stress components, and by adopting Voigt notation, leading to

$$\begin{pmatrix} e_{11} & e_{12} & 0 \\ 0 & 0 & e_{26} \\ 0 & 0 & 0 \end{pmatrix} = \begin{pmatrix} d_{11} & d_{12} & 0 \\ 0 & 0 & d_{26} \\ 0 & 0 & 0 \end{pmatrix} \times \begin{pmatrix} C_{11} & C_{12} & 0 \\ C_{21} & C_{22} & 0 \\ 0 & 0 & C_{66} \end{pmatrix}. \tag{6}$$

Thus, yielding

$$d_{12} = \frac{e_{12} \cdot C_{11} - e_{11} \cdot C_{12}}{C_{22} \cdot C_{11} - C_{21} \cdot C_{12}}, \tag{7}$$

$$d_{11} = \frac{e_{11} \cdot C_{22} - e_{12} \cdot C_{21}}{C_{11} \cdot C_{22} - C_{21} \cdot C_{12}}, \tag{8}$$

$$d_{26} = \frac{e_{26}}{C_{66}}. \tag{9}$$

The piezoelectric strain tensor of the chiral AFM Fe_2O_3 monolayer was systematically investigated using density functional perturbation theory (DFPT). Our calculations reveal a piezoelectric stress coefficient e_{11} of -17.99×10^{-10} C/m, significantly surpassing the value of 3.70×10^{-10} C/m of the MoS_2 monolayer, demonstrating stronger mechano–electric coupling. Combined with its remarkable mechanical stiffness, characterized by elastic constants $C_{11} = C_{22} = 167.21$ N/m and $C_{12} = C_{21} = 106.82$ N/m, the Fe_2O_3 monolayer yields a piezoelectric strain coefficient $d_{11} = -29.51$ pm/V. This value exceeds the documented d_{11} of 3.71 pm/V for the MoS_2 monolayer by a factor of eight [35, 36].

Moreover, the piezoelectric effect in the chiral AFM

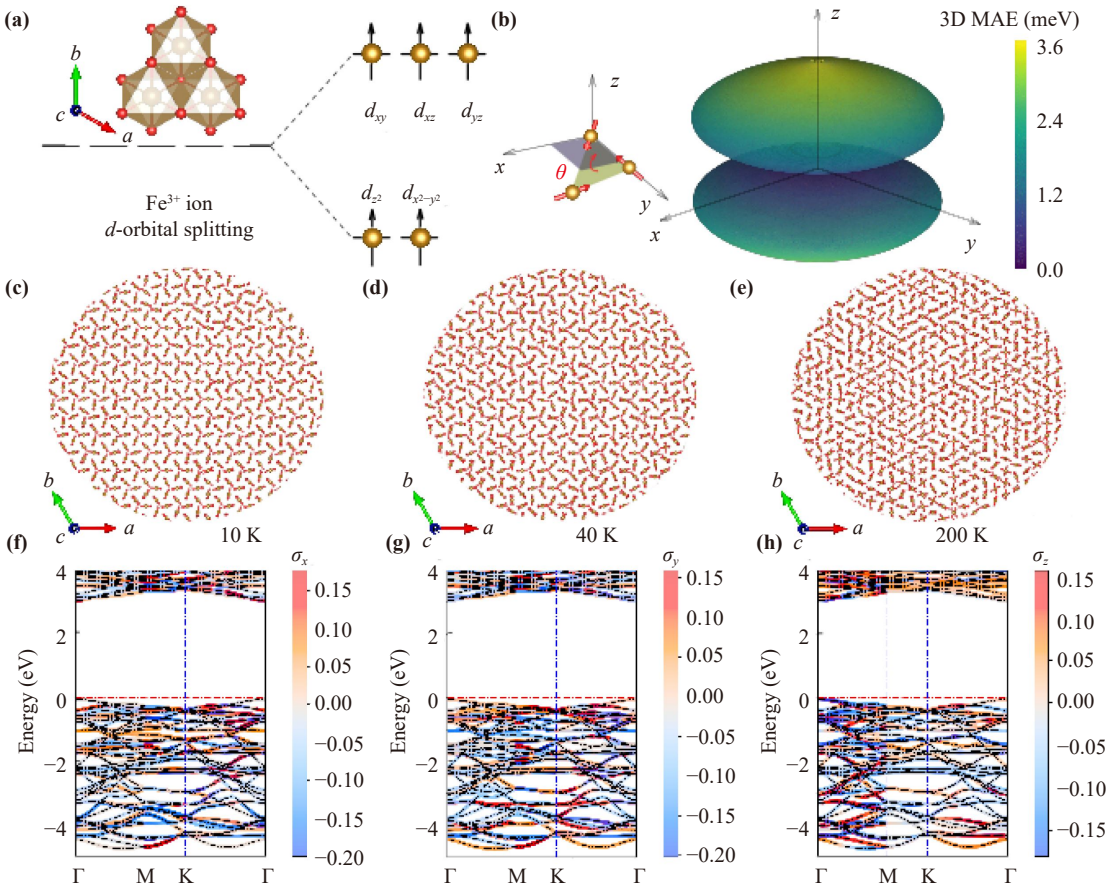

Fig. 3 **(a)** Splitting of Fe^{3+} 3*d* orbitals in an octahedral crystal field of the Fe_2O_3 monolayer. **(b)** 3D MAE surface plot of the chiral AFM state, in which the energies with in-plane magnetization are set to be zero. The inset defines the rotation angle (θ). Magnetic moment snapshots at **(c)** 10 K, **(d)** 40 K, and **(e)** 200 K. The corresponding band structures along high-symmetry lines in the Brillouin zone indicating in color the in-plane spin expectation values **(f)** $\langle\sigma_x\rangle$, **(g)** $\langle\sigma_y\rangle$, and **(h)** $\langle\sigma_z\rangle$. The color scale for the spin values is shown on the right.

Fe_2O_3 monolayer is highly sensitive to biaxial tensile strain (Fig. 4). Under 2% tensile strain, the coefficients d_{11} and e_{11} increase to -85.52×10^{-10} C/m and −22.06 pm/V, respectively. This enhanced piezoelectricity is primarily attributed to strain-induced relative displacements of the ionic sublattices. Furthermore, the chiral AFM order remains stable throughout the –6% to 2% in-plane biaxial strains (see Supplementary Materials Table S4), ensuring that the enhanced piezoelectric response originates purely from the electronic structure,

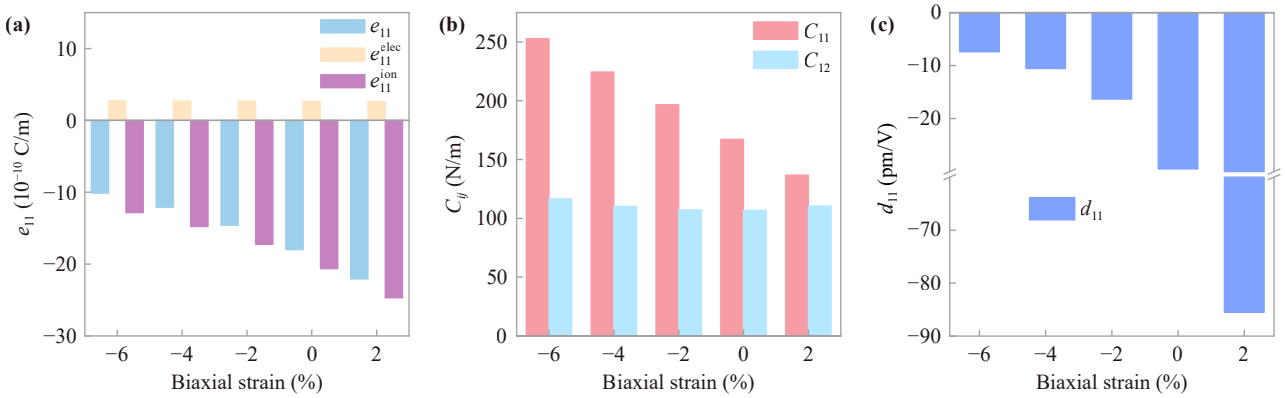

Fig. 4 **(a)** e_{11}, **(b)** C_{11}, C_{12} and **(c)** d_{11} as functions of biaxial strain along the *ab* direction from –6% to 2% in the Fe_2O_3 monolayer.

but not the magnetic phase transitions. The combination of this strain-tunable piezoelectricity with robust chiral AFM order suggests the potential for developing advanced strain-mediated, low-power spintronic devices and non-volatile magnetic memory with piezoelectric write capabilities.

3 Conclusion

In summary, we propose a viable experimental candidate for a 2D hexagonal Fe_2O_3 monolayer that simultaneously exhibits chiral AFM order, wide direct band gap, and pronounced piezoelectric response. The intrinsic Fe triangular frustrated lattice, along with a high magnetic anisotropy energy of 3.88 meV/Fe, jointly stabilizes the chiral AFM configuration. The interplay between structural inversion symmetry and magnetic time-reversal symmetry breaking gives rise to nontrivial spin-momentum locking and accounts for the in-plane piezoelectric response. Remarkably, the Fe_2O_3 monolayer exhibits a superior piezoelectric coefficient d_{11} of –29.51 pm/V, significantly exceeding that of the canonical MoS_2, with its performance further enhanced under tensile strain. These findings establish the hexagonal Fe_2O_3 monolayer as a promising platform for exploring magneto-electric coupling and potential applications in spintronic and multifunctional devices.

Declarations The authors declare no competing financial interest.

Electronic supplementary materials The online version contains supplementary material available at https://doi.org/10.15302/frontphys.2026.125203.

Acknowledgements This work was supported by the National Natural Science Foundation of China (Grant Nos. 22372142, 12304028, and 12404027), the Foreign Expert Introduction Program (Grant No. G2023003004L), the Central Guiding Local Science and Technology Development Fund Projects (Grant No. 236Z7605G), the Natural Science Foundation of Hebei Province (Grant Nos. B2024203051, A2024203023, A2024203002, and A2025203027), the Science and Technology Project of Hebei Education Department (Grant No. JZX2023020), the Innovation Capability Improvement Project of Hebei Province (Grant No. 22567605H), Hebei Province Yan Zhao Huang Jin Tai Talent Program (Postdoctoral Platform, B2025003011 and B2024003003), and the Ph.D. Research Startup Foundation of Hebei Normal University (Grant No. L2025B08).

References

1. D. D. Awschalom and M. E. Flatté, Challenges for semiconductor spintronics, *Nat. Phys.* 3(3), 153 (2007)
2. S. Dutta, A. K. Manna, and S. K. Pati, Intrinsic half-metallicity in modified graphene manoribbons, *Phys. Rev. Lett.* 102(9), 096601 (2009)
3. M. Ashton, D. Gluhovic, S. B. Sinnott, J. Guo, D. A. Stewart, and R. G. Hennig, Two-dimensional intrinsic half-metals with large spin gaps, *Nano Lett.* 17(9), 5251 (2017)
4. X. Jiang, Q. Liu, J. Xing, N. Liu, Y. Guo, Z. Liu, and J. Zhao, Recent progress on 2D magnets: Fundamental mechanism, structural design and modification, *Appl. Phys. Rev.* 8(3), 031305 (2021)
5. N. D. Mermin and H. Wagner, Absence of ferromagnetism or antiferromagnetism in one- or two-dimensional isotropic Heisenberg models, *Phys. Rev. Lett.* 17(22), 1133 (1966)
6. B. Huang, G. Clark, E. Navarro-Moratalla, D. R. Klein, R. Cheng, K. L. Seyler, D. Zhong, E. Schmidgall, M. A. McGuire, D. H. Cobden, W. Yao, D. Xiao, P. Jarillo-Herrero, and X. Xu, Layer-dependent ferromagnetism in a van der Waals crystal down to the monolayer limit, *Nature* 546(7657), 270 (2017)
7. Z. Fei, B. Huang, P. Malinowski, W. Wang, T. Song, J. Sanchez, W. Yao, D. Xiao, X. Zhu, A. F. May, W. Wu, D. H. Cobden, J. H. Chu, and X. Xu, Two-dimensional itinerant ferromagnetism in atomically thin Fe_3GeTe_2, *Nat. Mater.* 17(9), 778 (2018)
8. Z. Zhang, J. Shang, C. Jiang, A. Rasmita, W. Gao, and T. Yu, Direct photoluminescence probing of ferromagnetism in monolayer two-dimensional $CrBr_3$, *Nano Lett.* 19(5), 3138 (2019)
9. Z. X. Shen, C. Su, and L. He, High-throughput computation and structure prototype analysis for two-dimensional ferromagnetic materials, *npj Comput. Mater.* 8(1), 32 (2022)
10. J. Girovsky, J. Nowakowski, M. E. Ali, M. Baljozovic, H. R. Rossmann, T. Nijs, E. A. Aeby, S. Nowakowska, D. Siewert, G. Srivastava, C. Wäckerlin, J. Dreiser, S. Decurtins, S. X. Liu, P. M. Oppeneer, T. A. Jung, and N. Ballav, Long-range ferrimagnetic order in a two-dimensional supramolecular Kondo lattice, *Nat. Commun.* 8(1), 15388 (2017)
11. L. Liu, Q. Yu, J. Xia, W. Shi, D. Wang, J. Wu, L. Xie, Y. Chen, and L. Jiao, 2D air-stable nonlayered ferrimagnetic $FeCr_2S_4$ crystals synthesized via chemical vapor deposition, *Adv. Mater.* 36(25), 2401338 (2024)
12. X. Wang, K. Du, Y. Yang, F. Liu, P. Hu, J. Zhang, Q. Zhang, M. H. S. Owen, X. Lu, C. K. Gan, and P. Sengupta, Raman spectroscopy of atomically thin two-dimensional magnetic iron phosphorus trisulfide ($FePS_3$) crystals, *2D Mater.* 3(3), 031009 (2016)
13. K. Kim, S. Y. Lim, J. Kim, J. U. Lee, S. Lee, P. Kim, K. Park, S. Son, C. H. Park, J. G. Park, and H. Cheong, Antiferromagnetic ordering in van der Waals 2D magnetic material $MnPS_3$ probed by Raman spectroscopy, *2D Mater.* 6(4), 041001 (2019)
14. J. Zhang, J. Yang, L. Lin, and J. Zhu, An antiferromagnetic two-dimensional material: Chromium diiodides monolayer, *J. Semicond.* 41(12), 122502 (2020)
15. H. Sun, P. Dong, C. Wu, and P. Li, Multifield-induced antiferromagnet transformation into altermagnet and realized anomalous valley Hall effect in monolayer $VPSe_3$, *Phys. Rev. B* 111(23), 235431 (2025)
16. C. Wu, H. Sun, P. Dong, Y. Z. Wu, and P. Li, Coexisting triferroic and multiple types of valley polarization by

structural phase transition in 2D materials, *Adv. Funct. Mater.* 35(31), 2501506 (2025)
17. X. Hu, W. Zhao, W. Xia, H. Sun, C. Wu, Y. Z. Wu, and P. Li, Valley polarization and anomalous valley Hall effect in altermagnet Ti_2Se_2S with multipiezo properties, *Appl. Phys. Lett.* 127(1), 011905 (2025)
18. X. Zhang and S. Zhang, Sliding-induced ferrovalley polarization and possible antiferromagnetic half-metal in bilayer altermagnets, *Front. Phys. (Beijing)* 21(7), 075203 (2026)
19. X. Marti, I. Fina, C. Frontera, J. Liu, P. Wadley, Q. He, R. J. Paull, J. D. Clarkson, J. Kudrnovský, I. Turek, J. Kuneš, D. Yi, J. H. Chu, C. T. Nelson, L. You, E. Arenholz, S. Salahuddin, J. Fontcuberta, T. Jungwirth, and R. Ramesh, Room-temperature antiferromagnetic memory resistor, *Nat. Mater.* 13(4), 367 (2014)
20. T. Jungwirth, J. Sinova, A. Manchon, X. Marti, J. Wunderlich, and C. Felser, The multiple directions of antiferromagnetic spintronics, *Nat. Phys.* 14(3), 200 (2018)
21. L. Šmejkal, Y. Mokrousov, B. Yan, and A. H. MacDonald, Topological antiferromagnetic spintronics, *Nat. Phys.* 14(3), 242 (2018)
22. S. Hu, D. F. Shao, H. Yang, C. Pan, Z. Fu, M. Tang, Y. Yang, W. Fan, S. Zhou, E. Y. Tsymbal, and X. Qiu, Efficient perpendicular magnetization switching by a magnetic spin Hall effect in a noncollinear antiferromagnet, *Nat. Commun.* 13(1), 4447 (2022)
23. L. Song, F. Zhou, H. Li, B. Ding, X. Li, X. Xi, Y. Yao, Y. C. Lau, and W. Wang, Large anomalous Hall effect at room temperature in a Fermi-level-tuned Kagome antiferromagnet, *Adv. Funct. Mater.* 34(28), 2316588 (2024)
24. L. W. He, S. L. Yu, and J. X. Li, Variational Monte Carlo study of the 1/9-magnetization plateau in Kagome antiferromagnets, *Phys. Rev. Lett.* 133(9), 096501 (2024)
25. S. Wang, W. W. Wang, J. Fan, X. Zhou, X. P. Li, and L. Wang, Two-dimensional dual-switchable ferroelectric altermagnets: Altering electrons and magnons, *Nano Lett.* 25(40), 14618 (2025)
26. J. Xiong, J. Jiang, Y. Cui, H. Gao, J. Zhou, Z. Liu, K. K. Zhang, S. Cheng, K. Wu, S. W. Cheong, K. Chang, Z. Liu, H. Yang, S. J. Liang, B. Cheng, and F. Miao, All-electrical self-switching of van der Waals chiral antiferromagnet, *Phys. Rev. Lett.* 135(20), 206701 (2025)
27. S. Xu, B. Dai, Y. Jiang, D. Xiong, H. Cheng, L. Tai, M. Tang, Y. Sun, Y. He, B. Yang, Y. Peng, K. L. Wang, and W. Zhao, Universal scaling law for chiral antiferromagnetism, *Nat. Commun.* 15(1), 3717 (2024)
28. Y. Nambu, M. Ichihara, Y. Kiuchi, S. Nakatsuji, and Y. Maeno, Synthesis and characterization of the quasi-two-dimensional triangular antiferromagnets $Ni_{1-x}M_xGa_2S_4$ (M=Mn, Fe, Co, Zn), *J. Cryst. Growth* 310(7–9), 1881 (2008)
29. J. J. Zhang, L. Lin, Y. Zhang, M. Wu, B. I. Yakobson, and S. Dong, Type-II multiferroic $Hf_2VC_2F_2$ MXene monolayer with high transition temperature, *J. Am. Chem. Soc.* 140(30), 9768 (2018)
30. S. Li, F. Wang, Y. Wang, J. Yang, X. Wang, X. Zhan, J. He, and Z. Wang, Van der Waals ferroelectrics: Theories, materials, and device applications, *Adv. Mater.* 36(22), 2301472 (2024)
31. Q. Zhang, S. Zuo, P. Chen, and C. Pan, Piezotronics in two-dimensional materials, *InfoMat* 3(9), 987 (2021)
32. Y. Liu, E. T. N. Wahyudin, J. H. He, and J. Zhai, Piezotronics and piezo-phototronics in two-dimensional materials, *MRS Bull.* 43(12), 959 (2018)
33. L. Zhou, Y. Guo, Y. Su, and J. Zhao, Layered group-IV-V-VI semiconductors with superior piezoelectricity and ferroelectricity, *Front. Phys. (Beijing)* 21(9), 095202 (2026)
34. Y. Q. Li, Q. W. He, D. S. Tang, X. Shang, and X. C. Wang, Intrinsically asymmetric atomic character regulates piezoelectricity in two-dimensional materials, *Front. Phys. (Beijing)* 19(3), 33201 (2024)
35. K. A. N. Duerloo, M. T. Ong, and E. J. Reed, Intrinsic Piezoelectricity in two-dimensional materials, *J. Phys. Chem. Lett.* 3(19), 2871 (2012)
36. M. Noor-A-Alam and M. Nolan, Negative piezoelectric coefficient in ferromagnetic 1H-$LaBr_2$ monolayer, *ACS Appl. Electron. Mater.* 4(2), 850 (2022)
37. R. Bechmann, Elastic and piezoelectric constants of Alpha-quartz, *Phys. Rev.* 110(5), 1060 (1958)
38. R. Fei, W. Li, J. Li, and L. Yang, Giant piezoelectricity of monolayer group IV monochalcogenides: SnSe, SnS, GeSe, and GeS, *Appl. Phys. Lett.* 107(17), 173104 (2015)
39. C. K. Yang and L. Jiao, Superconducting two-dimensional FeSe grown on the Fe-enriched interface, *ACS Nano* 18(19), 12276 (2024)
40. D. Zhang, H. Wei, J. Duan, J. Chen, J. Chen, D. Yue, W. Gong, P. Liu, Y. Yang, J. Gou, J. Yan, K. Zhai, P. Wang, S. Hu, Z. Jia, W. Jiang, L. Liu, W. Wang, Y. Li, and Y. Jiang, Orbital torque switching of room temperature two-dimensional van der Waals ferromagnet Fe_3GaTe_2, *Nat. Commun.* 16(1), 7047 (2025)
41. T. Wang, W. Xue, H. Yang, Y. Zhang, S. Cheng, Z. Fan, R. W. Li, P. Zhou, and X. Xu, Robust ferrimagnetism and ferroelectricity in 2D ε-Fe_2O_3 semiconductor with ultrahigh ordering temperature, *Adv. Mater.* 36(35), 2311041 (2024)
42. Z. Jia, M. Zhao, Q. Chen, R. Sun, L. Cao, K. Ye, T. Zhu, L. Liu, Y. Tian, Y. Wang, J. Du, F. Zhang, W. Lv, F. F. Ling, Y. Zhai, Y. Jiang, and Z. Wang, Spin transport modulation of 2D Fe_3O_4 nanosheets driven by Verwey phase transition, *Adv. Sci. (Weinh.)* 11(41), 2405945 (2024)
43. B. Zhang, X. Chen, F. Deng, X. Lv, C. Zhang, B. Zheng, H. Wang, and J. Wang, Spin direction tunable topological transition in two-dimensional frustrate antiferromagnetic triangular lattice T-FeO_2 monolayer, *Appl. Phys. Lett.* 121(23), 232405 (2022)
44. B. Y. Zhang, K. Xu, Q. Yao, A. Jannat, G. Ren, M. R. Field, X. Wen, C. Zhou, A. Zavabeti, and J. Z. Ou, Hexagonal metal oxide monolayers derived from the metal–gas interface, *Nat. Mater.* 20(8), 1073 (2021)
45. M. N. Gjerding, A. Taghizadeh, A. Rasmussen, S. Ali, F. Bertoldo, T. Deilmann, N. R. Knøsgaard, M. Kruse, A. H. Larsen, S. Manti, T. G. Pedersen, U. Petralanda, T. Skovhus, M. K. Svendsen, J. J. Mortensen, T. Olsen,

and K. S. Thygesen, Recent progress of the Computational 2D Materials Database (C2DB), *2D Mater.* 8(4), 044002 (2021).

46. J. Madsen and T. Susi, The abTEM code: transmission electron microscopy from first principles, *Open Res. Eur.* 1, 24 (2021)
47. S. Bertolazzi, J. Brivio, and A. Kis, Stretching and breaking of ultrathin MoS_2, *ACS Nano* 5(12), 9703 (2011)
48. J. W. Jiang and H. S. Park, Mechanical properties of single-layer black phosphorus, *J. Phys. D Appl. Phys.* 47(38), 385304 (2014)
49. S. M. AL-Shomar, A. M. Quraishi, G. Nazir, A. Safeen, I. Shernazarov, A. Nurmuhammedov, V. Tirth, A. Algahtani, A. M. Alsuhaibani, R. M. Mohammed, M. S. Refat, N. M. A. Hadia, and A. Zaman, Unveiling elevated curie temperature and exceptional perpendicular magnetic anisotropy in chlorinated monolayer CrI_3, *Mater. Chem. Phys.* 328, 129994 (2024)
50. E. A. Zvereva, G. V. Raganyan, T. M. Vasilchikova, V. B. Nalbandyan, D. A. Gafurov, E. L. Vavilova, K. V. Zakharov, H. J. Koo, V. Y. Pomjakushin, A. E. Susloparova, A. I. Kurbakov, A. N. Vasiliev, and M. H. Whangbo, Hidden magnetic order in the triangular-lattice magnet Li_2MnTeO_6, *Phys. Rev. B* 102(9), 094433 (2020)
51. S. Yu, Y. Xu, Y. Dai, D. Sun, B. Huang, and W. Wei, Spin spiral order induced ferroelectricity in $MnRe_2O_8$ monolayer, *Phys. Rev. B* 108(17), 174429 (2023)
52. S. Mühlbauer, B. Binz, F. Jonietz, C. Pfleiderer, A. Rosch, A. Neubauer, R. Georgii, and P. Böni, Skyrmion lattice in a chiral magnet, *Science* 323(5916), 915 (2009)
53. Y. Chen, H. Chen, X. Shen, W. Chen, Y. Liu, Y. Wu, and Z. Yuan, Orbital-excitation-dominated magnetization dissipation and quantum oscillation of Gilbert damping in Fe films, *Phys. Rev. Lett.* 134(13), 136701 (2025)